Measurement of Charmed Meson Lifetimes at the KEK B Factory

Tomonobu Tomura
Department of Physics, University of Tokyo

January 11, 2000

Abstract

I report a measurement of D^+ lifetime using $0.25\,\text{fb}^{-1}$ of e^+e^- annihilation data taken near the $\Upsilon(4S)$ resonance with the BELLE detector at the KEK B factory. The D^+ lifetime is measured to be $0.82 \pm 0.13\,\text{ps}$. It is confirmed no significant systematic bias exists in the analysis.

Contents

Chapter 1

Introduction

The measurement of the systematics of charmed hadron lifetimes is significant for understanding heavy quark decays. For example, charmed meson ground states $D^+(c\bar{d})$, $D^0(c\bar{u})$, and $D_s^+(c\bar{s})$ are different in the flavor of the light antiquark. Although the weak decay of the charm quark is dominant for the decays of these charmed mesons, the lifetimes of these mesons are different. This indicates that the identity of the light antiquark also has an influence on the charmed meson decay. The large ratio of the D^+ and D^0 lifetimes ($\tau_{D^+}/\tau_{D^0} \sim 2.5$)[1] arises primarily from destructive interference between different quark diagrams that contribute significantly only to decay of the D^+. This interference, as well as a number of smaller effects, which can cause the D_s^+ and D^0 lifetimes differ, appear in a systematic expansion, in inverse powers of the charm quark mass, of the QCD contributions to the charm decay amplitudes. Precise measurement of charmed meson lifetimes is a good quantitative check of theories for heavy quark decays.

Precise measurement of charmed meson lifetimes is also important to understand the detector performance of the BELLE. A main aim of the KEK B factory is observation and measurement of CP violation in B meson decays. The $B^0 \rightarrow J/\psi K_S$ decay is the most promising mode for the measurement of CP violation, since the branching ratio of this mode is relatively large ($O(10^{-4})$) and the signal ($J/\psi \rightarrow l^+ l^-$, $K_S \rightarrow \pi^+ \pi^-$) is very clean. In this decay mode, the decay rate is expressed as

$$\frac{d\Gamma}{dt} = \frac{1}{2}e^{-\Delta\tau}\left(1 \pm \sin 2\phi_1 \cdot \sin x_d \Delta\tau\right) \tag{1.1}$$

$$\left(\Delta\tau \equiv \frac{\Delta t}{\tau_B} \approx \frac{\Delta z}{\gamma\beta c\tau_B}\right)$$

where Δz is the distance along the beam direction between the decay vertex positions of the $B^0 \rightarrow J/\psi K_S$ decay and the associated B decay. Since this time dependent asymmetry vanishes when integrated with time, it is crucial to measure Δz dependence of the decay rate. Systematics associated with Δz measurement have to be well understood. Since charmed meson lifetimes have

already been measured well in other experiments, comparison of our result with the world average allow us to evaluate the performance and systematics of the vertexing, in particular vertex detector and reconstruction software.

In this paper I describe measurement of D^+ lifetime based on the data collected at the KEK B factory.

Chapter 2

KEK B Factory

This chapter describes configuration of the KEKB accelerator and the BELLE detector.

2.1 KEKB Accelerator

The KEKB[2] is a high luminosity e^+e^- collider. It has two 3 km-long rings and provides an asymmetric energy collision of 8 GeV electron and 3.5 GeV positron. The arrangement of the two rings is shown in Figure 2.1. Its target luminosity
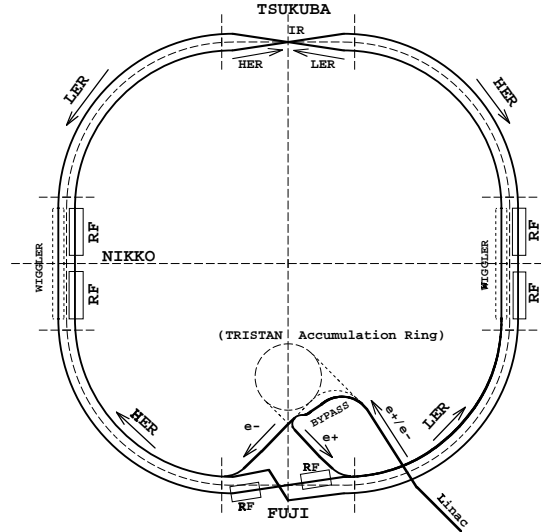

Figure 2.1: Arrangement of two rings at KEKB.

is $10^{34}/\mathrm{cm}^2/\mathrm{sec}$ to produce more than 100 million B meson pairs in a year.

To achieve the design luminosity, 5000 bunches have to be injected to each ring, where the bunch spacing is 0.6 m. To avoid the parasitic collisions near the interaction point, a finite angle beam crossing is chosen for KEKB with the crossing angle of ± 11 mrad. The designed beam sizes are $\sigma_x = 77\,\mu\mathrm{m}$, $\sigma_y = 1.9\,\mu\mathrm{m}$ and $\sigma_z = 4\,\mathrm{mm}$. The size in y coordinate is very small.

2.2 BELLE Detector

The BELLE detector[3] consists of following detectors as shown in Figure 2.2.
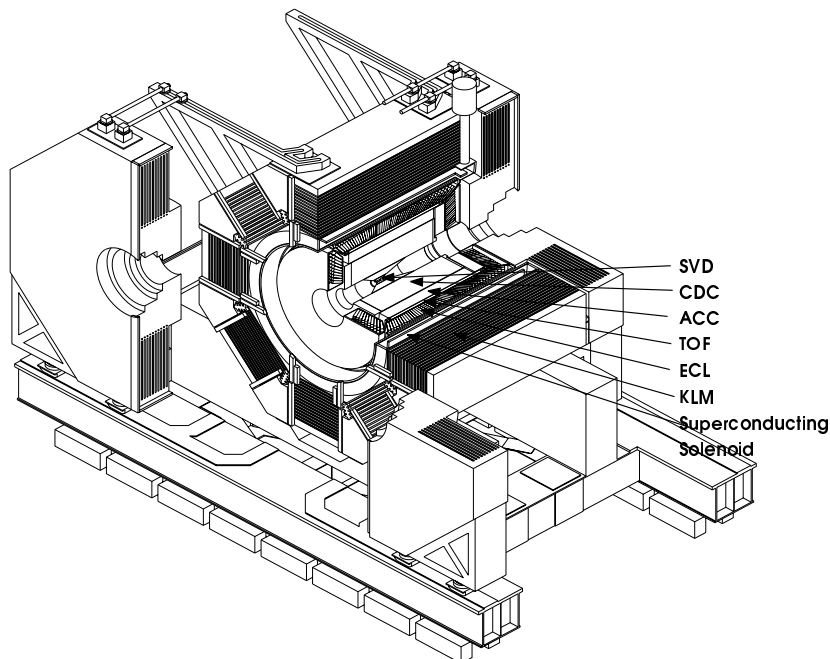

Figure 2.2: Schematic view of the BELLE detector

- Silicon Vertex Detector (SVD)

- Central Drift Chamber (CDC)

- Aerogel Čerenkov Counter (ACC)

- Time of Flight Counter (TOF)

- Electromagnetic Calorimeter (ECL)

- K_L/Muon Detector (KLM)

4

The SVD precisely measures the positions of the decay vertices. Charged tracks are primarily reconstructed by the CDC. The SVD will also help in the reconstruction of low p_T tracks. The CDC, TOF and ACC systems provide K/π separation up to 3.5 GeV/c. The CDC covers momenta up to 0.7 GeV/c, and the TOF covers the momenta up to 1.2 GeV/c while the ACC covers the momentum range $1.2 < p < 3.5$ GeV/c. The CDC and ECL identify electrons. The ECL also detects photons and measures their energy. The KLM detects K_Ls and muons. In particular, detection of the K_L from the $B^0 \to J/\psi K_L$ decay is important since it gives similar sensitivity to the CP asymmetry as the $B^0 \to J/\psi K_S$ decay.

2.2.1 SVD

The SVD is required to measure the B decay vertex better than 100 μm. The tracks produced at KEKB are rather soft and multiple-Coulomb scattering is a dominant source of the vertex resolution degradation. This imposes strict constraints on the detector design and mechanical layout. The innermost layer of the vertex detector must be placed as close to the interaction point as possible; the support structure must be low mass but stiff; and the readout electronics must be placed outside of the tracking volume. The last requirement is not a problem for the ϕ coordinate measurement, but for the z coordinate measurement it requires additional readout traces orthogonal to the z readout strips.

The CDC can reconstruct low momentum tracks down to p_T of about 70 MeV/c since the inner radius of the CDC is about 8 cm. The SVD is not required to function as a stand-alone tracker for low p_T tracks.

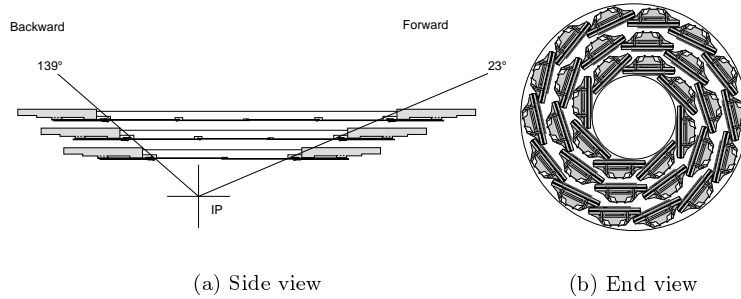(a) Side view   (b) End view

Figure 2.3: Side and end views of the BELLE SVD.

Figure 2.3 shows side and end views of the SVD. It consists of three layers in a barrel-only design and covers a solid angle 86 % of 4π. Each layer is constructed from independent ladders. Each ladder is constructed from double-sided silicon strip detectors (DSSDs) and reinforced by Boron-nitride support ribs. The three types of ladders consist of two types of half-ladders: short and long half-ladders.

5

The first layer ladder consists of two short half-ladders. The second layer ladder consists of one short and one long half-ladder. The third layer ladder consists of two long half-ladders. The short half-ladder is made of one DSSD and the long half-ladder is made of two DSSDs.

The arrangement of DSSDs and ladders for each layer is shown in Table 2.1.

Table 2.1: Arrangement of DSSDs and ladders for each layer.

Layer	1	2	3
Radius(mm)	30.0	45.5	60.5
# of ladders/layer	8	10	14
# of DSSDs/ladder	2	3	4

For the sensors, S6936 DSSDs fabricated by Hamamatsu Photonics, which were originally developed for the DELPHI experiment are used. They consist of 1280 sense strips and 640 readout pads on each side. All sense strips are biased via 25 MΩ polysilicon bias resister. The z strip pitch is 42 μm and the ϕ strip pitch is 25 μm. For the z coordinate determination, a double-metal structure is employed to readout the signal of orthogonal z sense strips along the beam axis. Adjacent strips are connected to one readout trace on the second metal layer. The n-side is chosen to be the z side and a p-stop structure is employed to isolate sense strips. However, relatively large thermal noise (measured to be about 600 electrons) is observed due to the "common" p-stop design. Every other sense strip is connected to readout pads on the ϕ side. Capacitive charge division readout is employed to readout signals from floating strips.

The VA1 frontend LSI chip manufactured by IDE AS in Norway is used to readout signals from DSSDs. It consists of preamplifier, shaper, sample/hold and analog multiplexer. A peaking time of 1 μs is chosen. It has 128 readout channels and 5 VA1 chips are put on a hybrid card to readout 640 channels of a DSSD. The number of total readout channels of the SVD is 81920.

Radiation tolerance is measured to be reasonably good. In particular, the measurements show that signal-to-noise ratios are expected to be greater than 10 up to 150 krad of radiation dose to both VA1 and DSSD[4].
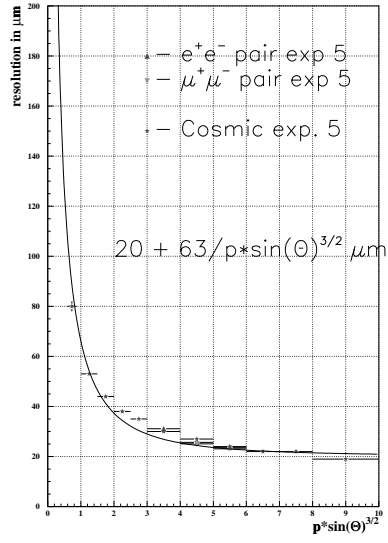
The backend electronics consists of a system of flash ADCs (analog-to-digital converters), DSPs (digital signal processors) and FPGA (field programmable gate array). The DSP provides common mode noise subtraction, data sparsification and data formatting at rates up to 500 Hz. Data processing is very flexible with this arrangement.

Figure 2.4 shows the impact parameter resolutions for 2 tracks events obtained from collision data and cosmic data in $r\phi$ and z. The resolution is

$$\sigma = 20 + 63/(p \cdot \sin^{3/2} \theta) \, \mu\text{m} \text{ (for } r\phi)$$
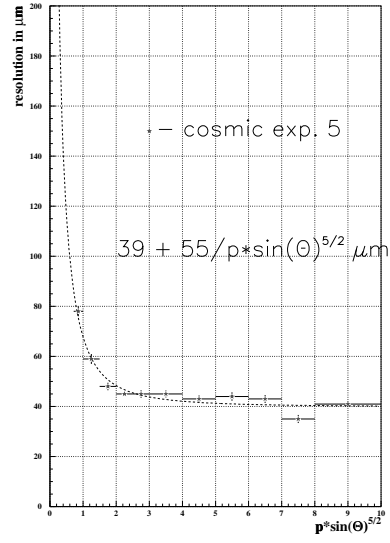$$\sigma = 39 + 55/(p \cdot \sin^{5/2} \theta) \, \mu\text{m} \text{ (for } z)$$

where the unit of the momentum p is GeV/c.

6

R-Phi Impact Parameter Resolution for 2 tracks events

Z Impact Parameter Resolution for 2 tracks events

$- e^+e^-$ pair exp 5
$- \mu^+\mu^-$ pair exp 5
$-$ Cosmic exp. 5

$- $ cosmic exp. 5

$20 + 63/p*\sin(\Theta)^{3/2} \; \mu m$

$39 + 55/p*\sin(\Theta)^{5/2} \; \mu m$

(a) $r\phi$ (b) $r\phi$

Figure 2.4: The impact parameter resolution of the BELLE SVD.

7

2.2.2 CDC

The CDC provides charged particle tracking and dE/dx measurements as well as fast charged-track information for the trigger.

The numbers of sense wires and cathode strips of the CDC are 8400 and 1792, respectively. There are two types of wires: one is an axial wire which is parallel to z axis; the other is a stereo wire which is tilted against z axis. The stereo angles range from 42.5 mrad to 72.1 $rmmrad$. The number of field wires is 24944 and the size of a drift cell is about 15 mm × 15 mm.

The CDC covers the $17° < \theta < 150°$ angular region (92 % of solid angle in $\Upsilon(4S)$ mass frame). It is 235 cm long. The inner and outer radii of the CDC are 9 cm and 86 cm, respectively. The CDC consists of 50 cylindrical layers of drift cells organized into 11 super-layers, where 6 of them are axial and 5 are stereo super-layers. Each super-layer contains between three and six layers. The CDC structure consists of three parts: the cathode part, which contains the three innermost layers of wires and cathodes; the inner part, which is a conical shaped region with a radius less than 280 mm, and a toroidally-shaped main part. The structure of the CDC is shown in Figure 2.5. He–C_6H_6 (50/50 %) gas is used
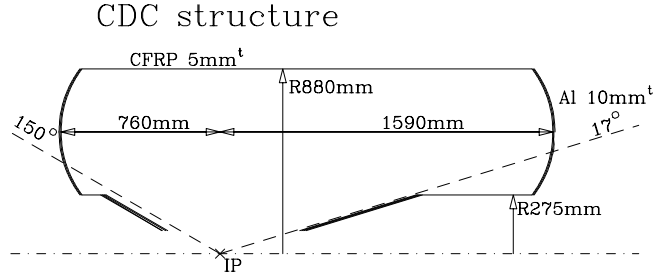
CDC structure

Figure 2.5: Side view of the CDC.

to minimize the multiple-Coulomb scattering. A magnetic field of 1.5 Tesla is chosen to minimize momentum resolution without sacrificing efficiency for low momentum tracks. As a result, the momentum resolution is expected to be $\sigma_p/p = 0.25\sqrt{1 + p^2}\,\%$.

The spatial resolution of the CDC is 140 μm for the Bhabha events. Figure 2.6 shows the p_T resolution in collision data. The resolution is

$$\sigma_{p_T}/p_T = 0.250 \times p_T \oplus 0.394\,\%$$

where the unit of p_T is GeV/c. Figure 2.7 shows the dE/dx performance of the BELLE CDC in collision data. The resolution of dE/dx is 8.3 % for hadrons and 5.7 % for electrons.

From the collision data and the current reconstruction software, the tracking efficiency is found to be 97 % above $p_T = 150$ MeV/c, and 60 % at $p_T = 50$ MeV/c. The efficiency degrades below $p_T = 150$ MeV/c since the minimum
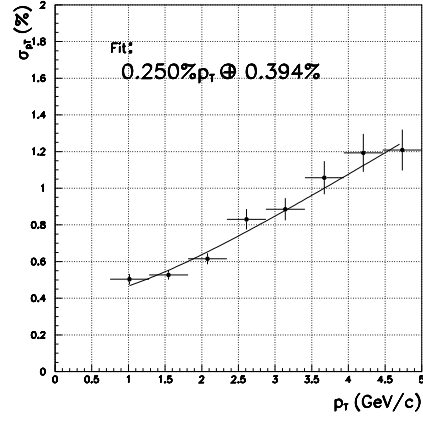
8

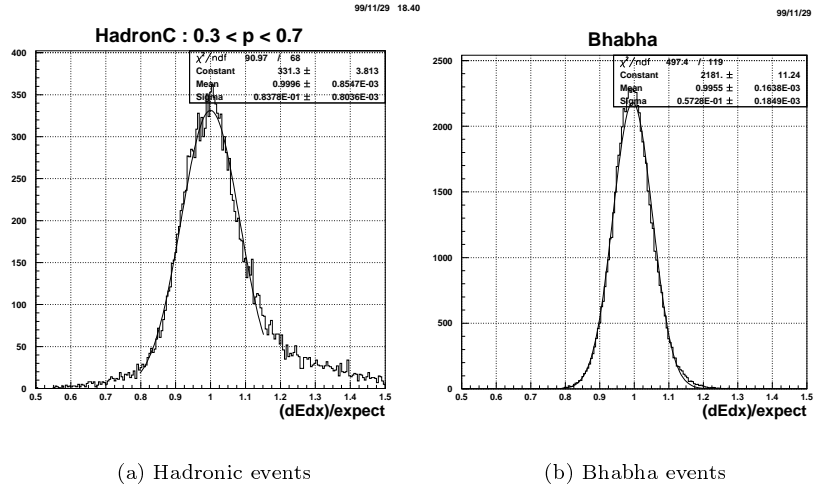Figure 2.6: The p_T resolution of the BELLE CDC in collision data.

(a) Hadronic events

(b) Bhabha events

Figure 2.7: The dE/dx resolution of the BELLE CDC in collision data.

radius of the stereo wire is $18\,\text{cm}$ and we loose z coordinate measurements for soft tracks. The SVD may improve the efficiency by providing z coordinate measurements. The matching efficiency between the SVD and the CDC is $97\,\%$. Tracks below $p_T = 0.07\,\text{GeV}/c$ cannot be reconstructed due to a geometrical limit.

2.2.3   ACC

The ACC system extends the coverage for particle identification (PID) upward from the $1.2\,\text{GeV}/c$ limit of the time-of-flight system to the kinematic limit of two-body B decays, i.e., to 2.5–$3.5\,\text{GeV}/c$, depending on polar angle.

The Čerenkov radiations occur in case of

$$n > \frac{1}{\beta} = \sqrt{1 + \left(\frac{m}{p}\right)^2}$$

where p is a measured momentum with the CDC and n is the refractive index of the matter. For example, when the particle with the momentum $p = 2\,\text{GeV}/c$ passes through the aerogel, if that particle is a pion (mass $m_\pi = 140\,\text{MeV}/c^2$) then $1/\beta = 1.002$. But if that particle is a kaon (mass $m_K = 494\,\text{MeV}/c^2$) then $1/\beta = 1.030$. Therefore, if the refractive index of the aerogel $n = 1.020$, the pion produces the Čerenkov radiation while the kaon does not.

Each aerogel counter module consists of the silica aerogel radiator module and fine-mesh photo-multiplier tubes (FM-PMTs) to detect Čerenkov radiation. The typical aerogel module comprises aerogel tiles contained in a 0.2-mm-thick aluminum box. The inner surface of the box is lined with Goretex sheet as the reflector.

The ACC is divided into two parts. A barrel array (BACC) occupies the volume bounded by $88.5 < r < 115\,\text{cm}$ and $-85 < z < 162\,\text{cm}$, and a forward endcap array (EACC) occupies the volume bounded by $42 < r < 114\,\text{cm}$ and $166 < z < 195\,\text{cm}$ as shown in Figure 2.8.

The BACC provides 3σ K/π separation in the momentum range $1.0 < p_K < 3.6\,\text{GeV}/c$. Table 2.2 shows the polar angle dependence of the refractive index (n), and the diameter and the number of the FM-PMTs for the barrel region. The refractive index of the aerogel is chosen so that the pion produces Čerenkov light in the aerogel while the kaon does not. Note that aerogel with a smaller refractive index is required at forward angles, where momenta are largest. Larger diameter phototubes are used at forward angles to compensate for the reduced light yield of the lower index material. The average material thickness is estimated to be $14\,\%$.

In the endcap region, a simple single-layer aerogel system with $n = 1.03$ is employed. This eliminates the need for an endcap TOF system, since $n = 1.03$ aerogel gives 3σ K/π separation in the momentum range $0.7 < p < 2.4\,\text{GeV}/c$. This approach provides complete endcap flavor tagging, as well as PID for many of the few-body decays relevant to CP studies.
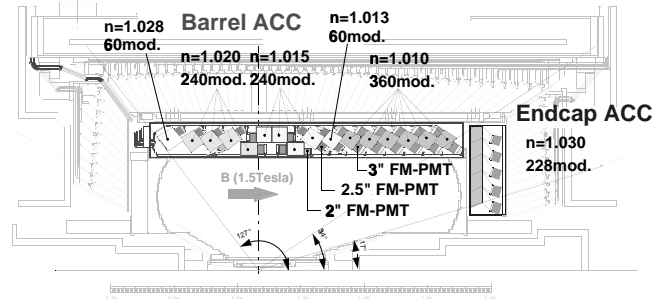
Figure 2.8: Configuration of the aerogel Čerenkov counter.

Table 2.2: Angle dependence of the refractive index (n), the PMT diameter and the number of the PMT.

Angle range	n	PMT diameter	# of PMT
33°−58°	1.010	76 mm	2
57°−64°	1.013	64 mm	2
63°−71°	1.015	64 mm	2
70°−78°	1.015	76 + 52 mm	2
77°−91°	1.015	76 mm	1
90°−99°	1.020	76 mm	1
98°−106°	1.020	64 + 52 mm	2
105°−121°	1.020	64 mm	1
120°−127°	1.028	64 mm	1

11

The barrel ACC consists of 960 modules: 15 modules in the z direction and 60 modules in azimuth as shown in Figure 2.8. The typical counter size is $12 \times 12 \times 12 \, \mathrm{cm}^3$, except for the 8th, 10th, and 12th from the front, which are slightly larger, i.e., $15 \times 12 \times 12 \, \mathrm{cm}^3$. The endcap ACC is a 228-element array arranged in five concentric rings with 60, 48, 48, 36 and 36 ϕ segments from outside to inside. A typical endcap counter is $12 \times 12 \, \mathrm{cm}^2$ in cross section and $10 \, \mathrm{cm}$ thick. The number of readout channels is 1560 in the barrel and 228 in the endcap.
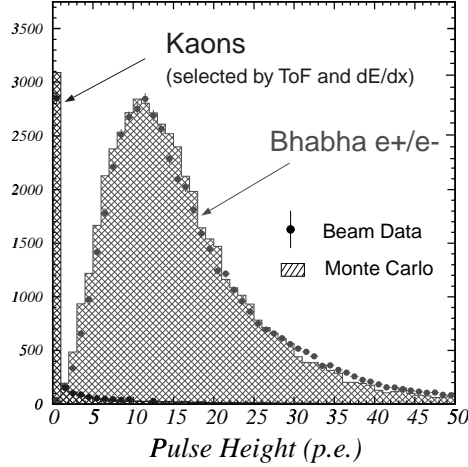

Figure 2.9: The pulse hight distribution of the ACC in the collision data.

Figure 2.9 shows the performance of the BELLE ACC obtained from the collision data. The pulse hight distribution shows a good agreement between data and MC.

2.2.4 TOF

The Time of Flight (TOF) system provides 3σ K/π separation up to $1.2 \, \mathrm{GeV}/c$ with a TOF time resolution of 100 ps. The following equation is satisfied using a measured time-of-flight T with the TOF and a measured momentum p with the CDC

$$ T = \frac{L}{c\beta} = \frac{L}{c} \sqrt{1 + \left(\frac{m}{p}\right)^2} $$

where L is a length of the flight. For example, when $L = 120 \, \mathrm{cm}$ and the particle with momentum $p = 1.2 \, \mathrm{GeV}/c$ flies into the TOF, if that particle is a pion ($m_\pi = 140 \, \mathrm{MeV}/c^2$) then $T = 4.03 \, \mathrm{ns}$, while if that particle is a kaon ($m_K = 494 \, \mathrm{MeV}/c^2$) then $T = 4.32 \, \mathrm{ns}$. The difference of T between π and K is $\sim 300 \, \mathrm{ps}$ and 3σ $K\pi$ separation is provided with the time resolution of 100 ps.

The TOF system comprises 64 barrel TOF/Trigger Scintillation Counter (TSC) modules. A TOF/TSC module consists of two trapezoidally shaped 4-cm-thick TOF counters and one 5-mm-thick TSC counter separated by a 2-cm gap as shown in Figure 2.10. The TOF/TSC modules are individually mounted to the inner wall of the CsI container at $r = 120$ cm. A coincidence between
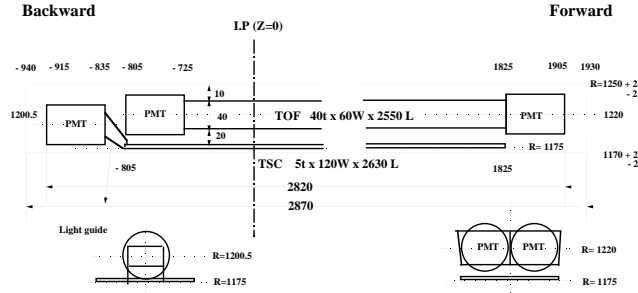

Figure 2.10: A TOF/TSC module.

TSC and TOF counters rejects γ background and provides a clean event timing to the BELLE trigger system.

The TOF is segmented into 128 ϕ sectors and readout by one fine-mesh photo-multiplier (FM-PMT) at each end. The TSC has 64 segments and is readout from only backward end by a single FM-PMT. The total number of readout channels is 256 for the TOF and 64 for the TSC. The TOF/TSC system covers an angular range of $34° < \theta < 121°$. The average material thickness of the TOF/TSC system is about 10 %.

Figure 2.11 shows the time resolution of the BELLE TOF system. The results achieve the time resolution that meets the BELLE design goal of 100 ps.

2.2.5   ECL

The main purpose of the electromagnetic calorimeter (ECL) is the detection of photons from B meson decays with high efficiency and good resolution. Most of the physics goals of the BELLE experiment require the reconstruction of exclusive B meson final states and many final states include π^0s. Almost all the π^0s decay in $\pi^0 \to \gamma\gamma$ mode. Thus it is important to have photon detection capabilities as much as charged particle detection, especially for low energy photon. π^0 mass resolution is dominated by the photon energy resolution. Sensitivity to and resolution of low energy photons are the critical parameters for the efficient π^0 detection.

And the electron identification in BELLE relies primarily on a comparison of the charged particle track momentum measured by the CDC and the energy it deposits in the ECL. Good energy resolution of the calorimeter results in better hadron rejection.
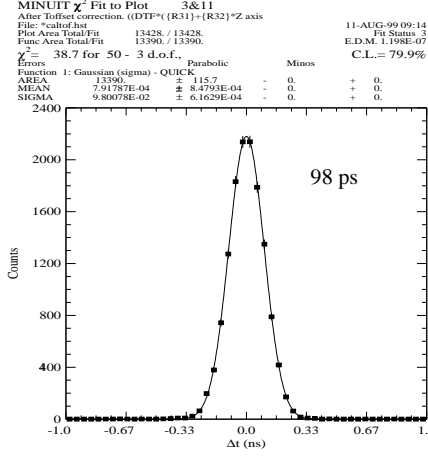
13

After Toffset correction. ((DTF*({R31}+{R32}*Z axis
File: *caltof.hst   11-AUG-99 09:14
Plot Area Total/Fit   13428. / 13428.   Fit Status 3
Func Area Total/Fit   13390. / 13390.   E.D.M. 1.198E-07
χ^2= 38.7 for 50 - 3 d.o.f.,   C.L.= 79.9%
Errors   Parabolic   Minos
Function 1: Gaussian (sigma) - QUICK
AREA   13390.   ± 115.7   - 0.   + 0.
MEAN   7.91787E-04   ± 8.4793E-04   - 0.   + 0.
SIGMA   9.80078E-02   ± 6.1629E-04   - 0.   + 0.

98 ps

Counts

Δt (ns)

Figure 2.11: The time resolution of the BELLE TOF system measured with the $\mu^+\mu^-$ events.

In order to satisfy these requirements, the ECL is designed based on the thallium-doped Cesium Iodide (CsI(Tl)) crystal. The BELLE ECL consists of 6624 barrel crystals, 1152 forward endcap crystals and 960 backward endcap crystals. All of crystals are $30\,\mathrm{cm}$ $(16.1X_0(\text{radiation length}))$ long. They are assembled into a tower structure. Each crystal is projected to the interaction point with a small tilt angle of $1.9°$ in both θ and ϕ directions to prevent any photon from escaping through the gaps between crystals. Figure 2.12 shows the structure of the ECL.

Each crystal is readout by two $10\,\mathrm{mm} \times 20\,\mathrm{mm}$ photodiodes (S2744-08). They are glued to the rear surface of the crystal via $1\,\mathrm{mm}$ thick acrylite plate since direct glue joints between the photodiode and the crystal often fails after heat cycles. The total readout channel is 17472.

The barrel crystals are installed in a honeycomb-like structure formed by $0.5\,\mathrm{mm}$ thick aluminum septum walls stretched between the inner and outer cylinders. The inner and outer cylinders, two endrings and the reinforcing bars form a rigid structure to support the weight of the crystals. They are made of stainless steel except the inner cylinder which is made of $1.5\,\mathrm{mm}$ thick aluminum to minimize the material in front of the calorimeter.

The energy resolution of the ECL is measured to be $\sigma_E/E = 2\,\%$ for the $e^+e^- \to \gamma\gamma$ events with the collision data. π^0 mass width is $\sim 5\,\mathrm{MeV}/c^2$. Good detection efficiency and good fake rejection for electrons above $500\,\mathrm{MeV}/c$ are obtained from collision data.
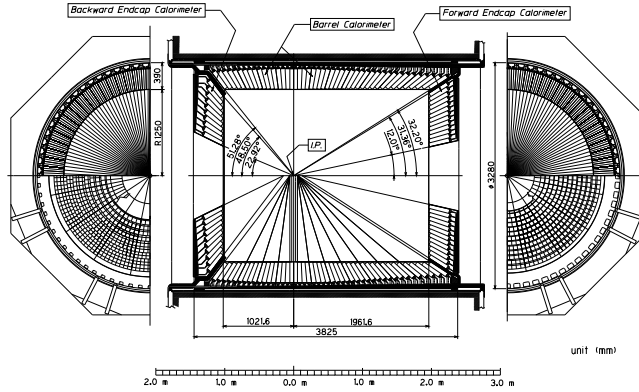
BELLE CsI ELECTROMAGNETIC CALORIMETER

Figure 2.12: The barrel and endcap parts of the ECL.

2.2.6 KLM

The KLM is designed to detect K_L and muons. The detection of K_L is needed to reconstruct $B^0 \to J/\psi K_L$. Muons are used in the CP violation measurements to identify the flavor tagging B meson and to reconstruct $J/\psi \to \mu^+\mu^-$. Energy measurement is not required since the muon momentum is measured by the CDC and the $B^0 \to J/\psi K_L$ decay kinematic constraints and the K_L direction gives adequate signal-to-noise ratio.

K_L is tagged with hadronic interactions in the ECL, the superconductor coil, or the KLM itself, while the μ does not induce the hadron shower.

The KLM is consists of barrel region and two endcap regions. The structure of both parts is a repetition of 47-mm-thick iron plates and 44-mm-thick slots. Resistive plate counter (RPC) modules are placed into those slots. There are 15 layers in the barrel and 14 layers in the endcap. The barrel is divided azimuthally into octants and the endcap is divided into quadrants. Figure 2.13 shows the structure of the barrel and endcap parts of the KLM. The iron plate is an absorber material for the KLM and also serves as a return path of the magnetic flux provided by the solenoid magnet.

The barrel part consists of 240 modules. The barrel RPC modules are rectangular in shape with external thicknesses and lengths of 34 mm and 2207 mm, respectively. The external width varies from 1542 mm to 2697 mm depending on the radial position of the module. Two barrel modules are placed into one slot, one for $+z$, the other for $-z$.

The endcap part consists of 112 modules. All endcap modules are the same size.

An RPC is essentially a planar spark counters wherein the avalanche induced by an incident charged particle is quenched when the limited amount of charge on the inner surface of highly resistive electrode is exhausted. The RPC is locally
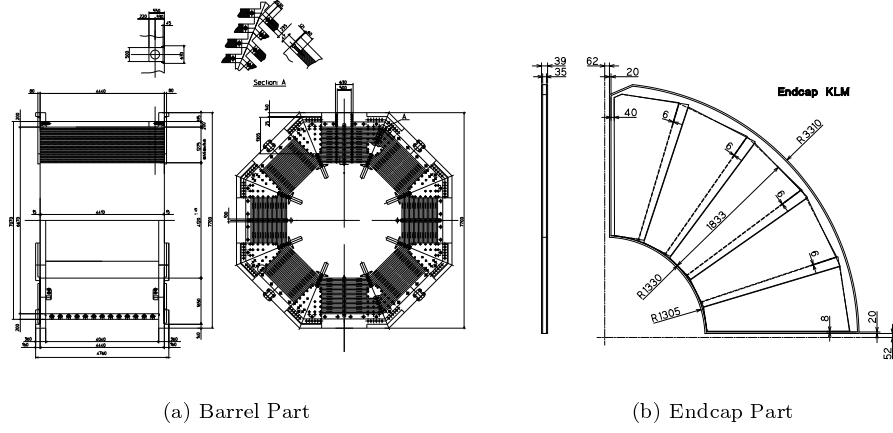
15

(a) Barrel Part

(b) Endcap Part

Figure 2.13: The barrel and endcap parts of the BELLE KLM.

deadend until the inner surfaces can recharge through the resistive material of the plates. As the resistive material for RPC, BELLE KLM employs glass, which has a bulk resistivity of about $10^{12}-10^{13}\,\Omega\,\mathrm{cm}$. Since the highly resistive HV electrodes are effectively transparent to the fast image pulses ($\sim 20\,\mathrm{ns}$) from the discharges, external electrodes can be used to sense the signals. The induced pulses are typically several tens of mV into $50\,\Omega$ resistor, eliminating the need for preamplifiers.

Each RPC module (superlayer) consists of two RPC layers. The readout for each superlayer consists of sets of orthogonal strips (typically 5 cm wide). In the barrel region, those strips provide ϕ and z measurements while they provide ϕ and r measurements in the endcap region. The number of readout channels is 21856 in barrel and 16218 in endcap. If a single RPC fires, both readout planes will see signals. Thus if the single-layer inefficiency is η, the inefficiency for the superlayer layer will be η^2. Typically, η is 10 %.

From collision data good detection efficiency and good fake rejection for muons above $800\,\mathrm{MeV}/c$ is obtained.

Chapter 3

Analysis

This chapter describes how D^+ lifetime is measured and shows the result of the analysis. The analysis is based on $0.25\,\mathrm{fb}^{-1}$ of e^+e^- annihilation data collected near the $\Upsilon(4S)$ resonance with the BELLE detector from October to December 1999. Results of a Monte Carlo sample are also shown for comparison. The MC sample consists of 3 million continuum events and 1 million $B\bar{B}$ events corresponding to about $1\,\mathrm{fb}^{-1}$.

D^+ candidates are reconstructed using $D^{*+} \to D^+\pi_s^0$, $D^+ \to K^-\pi^+\pi^+$ decay chain[1]. D^{*+} reconstruction is required to clean up D^+ candidates. The D^+ decay vertex is reconstructed using kinematic fit. The production point of the D^+ candidate is obtained extrapolating the reconstructed D^+ track into the interaction point (IP) profile. D^+ proper time is calculated from its decay length and momentum. The D^+ lifetime is extracted by fitting the D^+ proper-time distribution with lifetime function convoluted by resolution function.

3.1 Reconstruction

In this section I describe D^+ candidate selection and reconstruction of the decay vertex and the production point of the D^+ candidate.

Hadronic events are selected first to reject junk events. After D^+ candidates are reconstructed using $D^+ \to K^-\pi^+\pi^+$ decay mode, D^+ decay point is calculated using kinematic fit with vertex constraint. D^+ production point is calculated using pseudo D^+ track and IP profile.

3.1.1 Event Selection

Hadronic events are selected using the criteria listed in Table 3.1. Radial component of primary event vertex(V_r) should be less than $1.5\,\mathrm{cm}$ and z component(V_z) should be within $\pm3.5\,\mathrm{cm}$ to reject beam-wall and beam-gas events. Number of

---

[1]Charge conjugate modes are implied throughout this paper.

Table 3.1: Selection criteria for Hadronic events

Quantity	Criterion
Primary event vertex	$V_r < 1.5\,\mathrm{cm}$, $|V_z| < 3.5\,\mathrm{cm}$
# of good tracks	$\geqq 5$
E_{vis}	$\geqq 50\,\%$ of E_{cm}
$|P_z^*|$	$\leqq 30\,\%$ of E_{cm}
E_{sum}	$2.5\,\%$ of $E_{cm} \leqq E_{sum} \leqq 90\,\%$ of E_{cm}

good tracks should be greater than or equal to 5. Total visible energy E_{vis} (defined as sum of charged track momenta and cluster energies) calculated in the $\Upsilon(4S)$ rest frame should be greater than or equal to $50\,\%$ of the center of mass energy E_{cm}. Absolute value of z component sum for charged track momenta and cluster energies in the $\Upsilon(4S)$ rest frame $|P_z^*|$ should be less than or equal to $30\,\%$ of E_{cm}. Also sum of the ECL cluster energy E_{sum} should be between $2.5\,\%$ and $90\,\%$ of E_{cm}. These cuts are applied to eliminate Bhabha, $\mu^+\mu^-$, and other background events.

D^+ in $B\bar{B}$ events should not be used since those D^+ mesons are produced at B decay points, not e^+e^- interaction point. Ratio of 2$^{\mathrm{nd}}$ to 0$^{\mathrm{th}}$ Fox-Wolfram moments R_2 is used to reject $B\bar{B}$ events. The R_2 is defined as the ratio

$$R_2 = H_2/H_0 \tag{3.1}$$

where the $i$$^{\mathrm{th}}$ Fox-Wolfram moment H_i is defined as

$$H_i \equiv \sum_{j,k} \frac{|\vec{p}_j^*||\vec{p}_k^*|}{E^2} P_i\left(\cos\phi_{jk}\right). \tag{3.2}$$

The indices j,k run over all tracks in the event, $\vec{p}_j^*$ is the momentum vector of the track j in the $\Upsilon(4S)$ rest frame, E is the total energy of the event, ϕ_{jk} is the angle between the tracks j and k, and P_i is the $i$$^{\mathrm{th}}$ Legendre polynomial. This value is close to 1 when the event is jet-like. For the isotropic event the value is close to 0. Figure 3.1 shows the distribution of R_2 for continuum and $B\bar{B}$ events in Monte Carlo. I accept events with R_2 greater than 0.2. This cut eliminates more than $60\,\%$ of $B\bar{B}$ events while retaining more than $90\,\%$ of continuum events.

3.1.2 Charmed Meson Candidate

D^+ candidates are reconstructed using the $D^+ \to K^-\pi^+\pi^+$ decay mode.

I select the charged tracks which have at least 2 hits in both SVD $r\phi$ and z strips to ensure precise measurement of D^+ decay vertices. If kaon probability for a track is greater than or equal to 0.6, it is regarded as K. Otherwise it is regarded as π. Detail of the kaon probability calculation is described in section A.2.
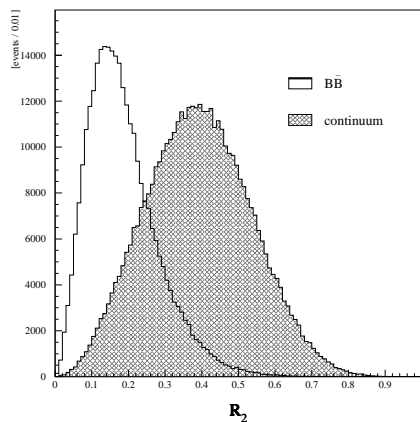
Figure 3.1: R_2 distribution for continuum and $B\bar{B}$ events

I form D^+ candidate using $K^-\pi^+\pi^+$ combinations. Since the charged tracks forming a D^+ candidate are required to originate from a common D^+ decay vertex, vertex constraint fit is applied to these tracks. (See section A.1 for details of the vertex fit.) I reject combinations with failed vertex fit. The 4-momentum of the D^+ candidate is obtained from the sum of the fitted momenta of the daughter tracks. I reject combinations with failed vertex fit with D^+ mass constraint. I retain D^+ candidate with a $K^-\pi^+\pi^+$ invariant mass from $1.80\,\mathrm{GeV}/c^2$ to $1.94\,\mathrm{GeV}/c^2$ for subsequent analysis.

For background suppression, a soft pion π_s^0 is required to form a D^{*+} with the D^+ candidate. π^0 is reconstructed from photon pairs detected in the ECL. The momentum of the photon is calculated on the assumption that the photon comes from the origin of the detector. The photon is required to have an energy greater than or equal to $20\,\mathrm{MeV}$. π^0 invariant mass is required to be within three standard deviations of the measured mean value of π^0 mass. π^0 mass constraint fit is applied to improve momentum resolution of the π^0 candidate. The 4-momentum of the D^{*+} is reconstructed by adding the reconstructed D^+ 4-momentum and π^0 momentum. To eliminate the $D^{(*)+}$ from $B\bar{B}$ background, I require that the momentum of D^{*+} in the $\Upsilon(4S)$ rest frame (p^*) is greater than $2.5\,\mathrm{GeV}/c$. $p^*(D^{*+})$ distributions for continuum and $B\bar{B}$ events in Monte Carlo are shown in Figure 3.2. Since $2.5\,\mathrm{GeV}/c$ is the upper limit of the $p^*(D^{*+})$ in the $B\bar{B}$ events, almost all the D^+ backgrounds from the $B\bar{B}$ events are rejected by this requirement. 70 % of the D^{*+} in the continuum events remains after the p^* cut.

$D^{*+}-D^+$ mass difference distributions from the data and Monte Carlo sample after above cuts are shown in Figure 3.3. We have more background in the data distribution than the MC distribution because π^0 selection criteria are not
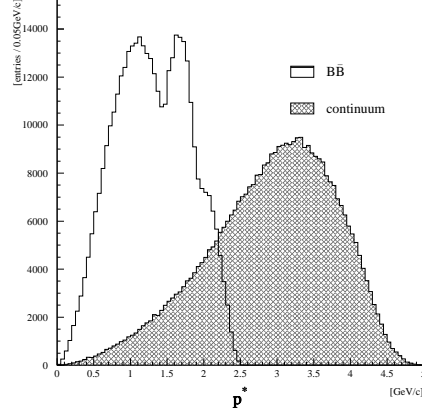
19

Figure 3.2: p^* (the momentum in the $\Upsilon(4S)$ rest frame) of D^{*+} for continuum and $B\bar{B}$ event
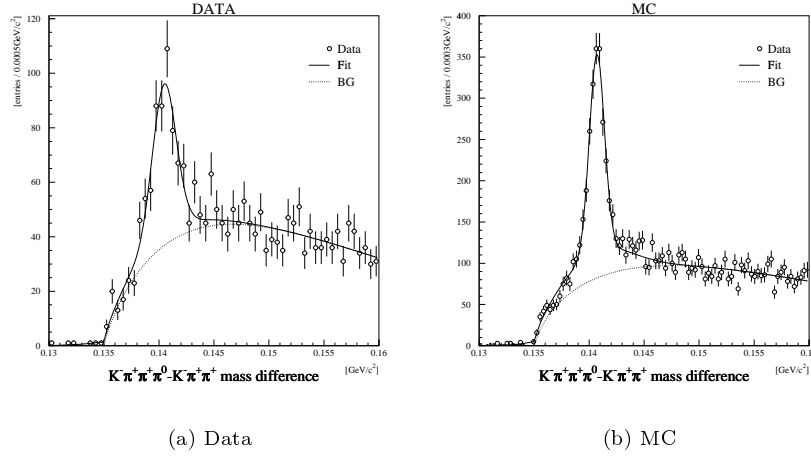

(a) Data

(b) MC

Figure 3.3: $D^{*+}-D^+$ mass difference distributions for the $D^{*+} \rightarrow D^+\pi_s^0$, $D^+ \rightarrow K^-\pi^+\pi^+$ candidates from the data and the MC. Points with error bar represent data. A solid line represents the fit result. A dotted line represents the background function.

optimized yet for the data. I fit the $D^{*+}-D^+$ mass difference distribution with a sum of two Gaussians with a same mean value for signal plus a threshold function for background;

$$
\rho(\Delta m) = \underbrace{A\left[\frac{f}{\sqrt{2\pi}\sigma_1}\exp\left\{-\frac{(\Delta m-\mu)^2}{2\sigma_1^2}\right\} + \frac{1-f}{\sqrt{2\pi}\sigma_2}\exp\left\{-\frac{(\Delta m-\mu)^2}{2\sigma_2^2}\right\}\right]}_{\text{signal}}
$$
$$
+ \underbrace{(\Delta m - \Delta M_0)^\alpha \exp\left\{c_0 + c_1(\Delta m - \Delta M_0)\right\}}_{\text{background}}. \quad (3.3)
$$

$$
(\Delta m \equiv m_{K^-\pi^+\pi^+\pi^0} - m_{K^-\pi^+\pi^+})
$$
$$
(\sigma_1 < \sigma_2)
$$

The fit results are listed in Table 3.2. The D^{*+}–D^+ mass difference is required to be within $2.5\,\sigma_1$ from the mean value. If we have more than one D^{*+} candidate in one event, the candidate with Δm closest to the mean value is selected.

Table 3.2: Parameters obtained from the fit to the $D^{*+}-D^+$ mass difference distributions.

Parameter	Data	MC
μ	$140.5\pm0.1\,\mathrm{MeV}/c^2$	$140.71\pm0.03\,\mathrm{MeV}/c^2$
σ_1	$1.1\pm0.1\,\mathrm{MeV}/c^2$	$0.69\pm0.04\,\mathrm{MeV}/c^2$
A_1	374 ± 61	2188 ± 135
σ_2	$3.9\pm2.0\,\mathrm{MeV}/c^2$	$3.0\pm0.2\,\mathrm{MeV}/c^2$
f	0.79 ± 0.15	0.62 ± 0.06
ΔM_0	$135.0\pm0.2\,\mathrm{MeV}/c^2$	$135.11\pm0.07\,\mathrm{MeV}/c^2$
α	0.85 ± 0.05	0.68 ± 0.02
c_0	8.5 ± 0.4	8.3 ± 0.2
c_1	$-73\pm11\,(\mathrm{GeV}/c^2)^{-1}$	$-55\pm5\,(\mathrm{GeV}/c^2)^{-1}$
χ^2/DOF	$41/43$	$101/88$

$K^-\pi^+\pi^+$ invariant mass distributions with all cuts applied are shown in Figure 3.4. I fit the $K^-\pi^+\pi^+$ invariant mass distribution with a Gaussian for signal plus a linear background:

$$
f(m_{K^-\pi^+\pi^+}) = \underbrace{\frac{A}{\sqrt{2\pi}\sigma}\exp\left\{-\frac{(m_{K^-\pi^+\pi^+}-\mu)^2}{2\sigma^2}\right\}}_{\text{signal}}
$$
$$
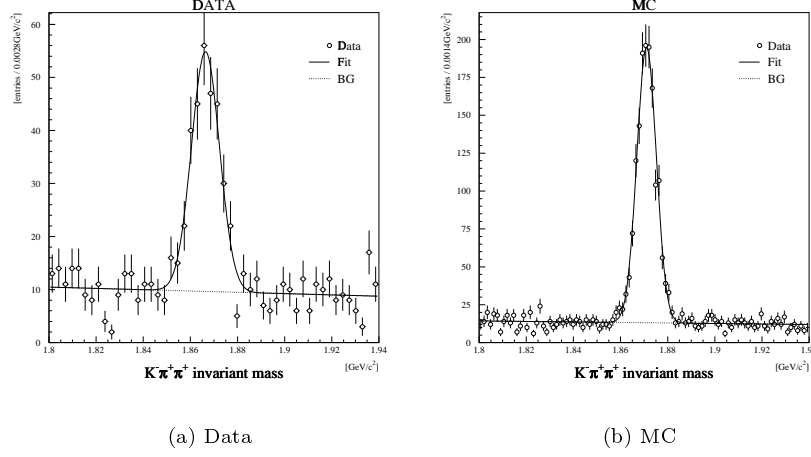+ \underbrace{C_0 + C_1 m_{K^-\pi^+\pi^+}}_{\text{background}}. \quad (3.4)
$$

(a) Data   (b) MC

Figure 3.4: The $K^-\pi^+\pi^+$ invariant mass distribution for the $D^{*+} \to D^+\pi_s^0$, $D^+ \to K^-\pi^+\pi^+$ candidates of the data and MC. Points with error bar represents data. A solid line represents the fit result. A dotted line represents the background function.

Table 3.3: Parameters obtained from the fit to the D^+ candidate invariant mass distributions.

Parameter	Data	MC
μ	1.8664±0.0006 GeV/c^2	1.8710±0.0002 GeV/c^2
σ	5.9±0.5 MeV/c^2	4.1±0.2 MeV/c^2
A	240±20	1340±40
C_0	33±6	44±5
C_1	$-13\pm3\,(\mathrm{GeV}/c^2)^{-1}$	$-17\pm3\,(\mathrm{GeV}/c^2)^{-1}$
χ^2/DOF	93/45	105/95

The fit results are listed in Table 3.3. I use the D^+ candidates with the D^+ mass within $\pm 6\sigma$ from the mean value for lifetime fit. The D^+ mass sideband region is included in the fit to model the background function as described in the section 3.2.

Selection requirements are summarized in Table 3.4.

Table 3.4: Selection requirements for D^+ candidates

Quantity	Criterion
# of $r\phi$ SVD hits	$\geqq 2$
# of z SVD hits	$\geqq 2$
kaon probability	$\geqq 60\,\%$ for K
	$< 60\,\%$ for π
$|\Delta m - \mu|$	$< 2.5\,\sigma_1$
$p^*(D^{*+})$	$> 2.5\,\mathrm{GeV}/c$

3.1.3 Production Point Reconstruction

D^+ production point is reconstructed by extrapolating pseudo D^+ track back into the IP profile as shown in Figure 3.5.
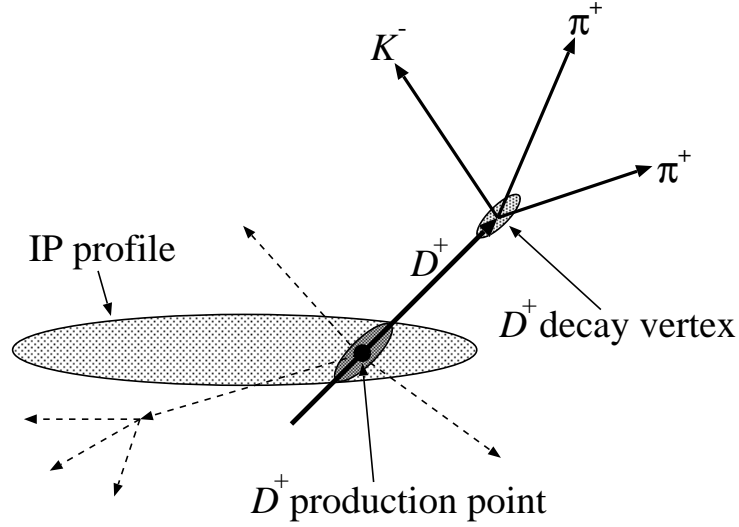
Figure 3.5: Schematic drawing of the production point reconstruction from the D^+ track and the IP profile.

The IP profile is calculated run-by-run using the hadronic data described in section 3.1.1. Initially primary event vertex is calculated using all tracks available. The primary event vertex is recalculated using all tracks consistent with the initial primary vertex. Three-dimensional distribution of the primary vertex is fitted with 3-dimensional Gaussian to obtain IP position and size. The 3-dimensional fit takes into account the effect of the ± 11 mrad crossing angle. Since vertex resolutions for the x and y directions are comparable to or larger than the true IP sizes, the beam size measurement of the accelerator group is used to determine the IP size for the x and y directions.

D^+ production point is calculated from the reconstructed D^+ track and the IP profile using vertex constraint fit with IP constraint (cf. section A.1).

3.2 Lifetime Fit

This section describes calculation of D^+ proper time and extraction of the D^+ lifetime from the proper-time distribution.

3.2.1 Proper Time Calculation

Proper time t is calculated from the decay vertex $\vec{r}_{\text{dec}}$, the production point $\vec{r}_{\text{IP}}$, and the D^+ momentum $\vec{p}$. Generally, the decay length l_{dec} is calculated as the projection of the distance between $\vec{r}_{\text{dec}}$ and $\vec{r}_{\text{IP}}$ onto $\vec{p}$.

$$l_{\text{dec}} = (\vec{r}_{\text{dec}} - \vec{r}_{\text{IP}}) \cdot \frac{\vec{p}}{|\vec{p}|} \tag{3.5}$$

The proper time t is presented using D^+ mass m and light speed c as

$$
\begin{aligned}
t &= \frac{m}{c} \frac{l_{\text{dec}}}{p} \\
&= \frac{m}{c} \frac{(\vec{r}_{\text{dec}} - \vec{r}_{\text{IP}}) \cdot \vec{p}}{p^2} .
\end{aligned}
\tag{3.6}
$$

It is expected that the measurement along y direction is most significant because of small IP size in the y direction. I check this hypothesis by looking at the significance $SIG = t_{\text{rec}}/|t_{\text{rec}} - t_{\text{gen}}|$ where t_{rec} is the reconstructed proper time and t_{gen} is the proper time from the generator information for following cases:

- Only y direction information is used. (1D)

- The proper time is calculated in the xy plane. (2D)

- The z direction information is also used. (3D)

The SIG distributions are shown in Figure 3.6. Mean values of the SIG are listed in Table 3.5.
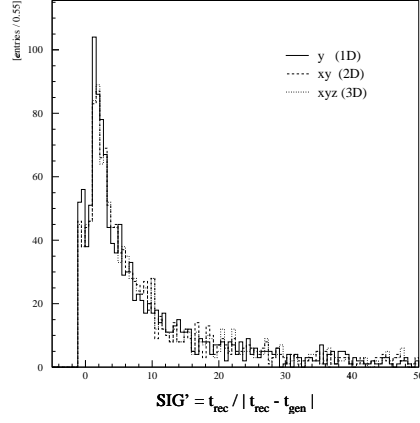
Figure 3.6: The distributions of the significance $SIG = t_{\mathrm{rec}}/|t_{\mathrm{rec}} - t_{\mathrm{gen}}|$. The solid, dashed, dotted histograms represent the SIG distributions for y, xy and xyz, respectively.

Table 3.5: The mean values of the significance $SIG = t_{\mathrm{rec}}/|t_{\mathrm{rec}} - t_{\mathrm{gen}}|$.

Dimension	Mean of SIG
y only (1D)	8.73
xy (2D)	9.14
xyz (3D)	9.07

There is no significant difference among three cases. Since the first case is expected to have least systematic uncertainties, I use only one-dimensional information along y axis for this analysis. The proper time t becomes

$$t = \frac{m}{c} \frac{(r_{\text{dec}\,y} - r_{\text{IP}\,y})}{p_y} \, . \tag{3.7}$$

The lifetime measurement in z direction can be compared with the measurement in y direction to evaluate the vertexing performance in z direction.

3.2.2 Extraction of D^+ Lifetime

Unbinned maximum likelihood fit to the proper-time distribution is used to extract the D^+ lifetime. Probability density function ρ for the proper time t_i is expressed as

$$\rho\left(t_i\right) = \int_0^\infty L(t') \, R(t_i - t') \, dt' \, . \tag{3.8}$$

$L(t')$ represents a lifetime term and $R(t_i - t')$ represents a resolution term.

If there is no background the lifetime term becomes

$$E\left(t|\tau\right) \equiv \frac{1}{\tau} \exp\left(-\frac{t}{\tau}\right) \, . \tag{3.9}$$

In reality background contributions has to be taken into account. The background events are considered as the mixture of $c\bar{c}$ events, $u\bar{u}$, $d\bar{d}$, $s\bar{s}$ events, and few $b\bar{b}$ events. The uds events have zero lifetime while the $c\bar{c}$ (and $b\bar{b}$) events have some lifetime. To fit with the background I approximate the background proper-time distribution as the sum of the fraction of the background $f_{\tau_{BG}}$ which has a lifetime τ_{BG} and the fraction $(1-f_{\tau_{BG}})$ which has zero lifetime. The background proper-time distribution is described as $(f_{\tau_{BG}} E(t|\tau_{BG}) + (1 - f_{\tau_{BG}})\delta(t))$.

Introducing signal probability of each event $p_{sig,i}$ lifetime term can be expressed as

$$L(t') = p_{sig,i} E(t'|\tau_{sig}) + (1 - p_{sig,i}) \left\{ f_{\tau_{BG}} E(t'|\tau_{BG}) + (1 - f_{\tau_{BG}})\delta(t') \right\} \, . \tag{3.10}$$

where τ_{sig} is a lifetime of signal events, i.e. D^+ lifetime. $p_{sig,i}$ is calculated from the D^+ mass. The D^+ mass distribution is fitted with a Gaussian (G) for signal and a first order polynomial $(P1)$ for background as shown in Figure 3.4. Using these functions p_{sig} can be expressed as;

$$p_{sig}(m_{K^- \pi^+ \pi^+}) = \frac{G}{G + P1} \, . \tag{3.11}$$

Figure 3.7 shows the p_{sig} distributions for the data and MC samples.

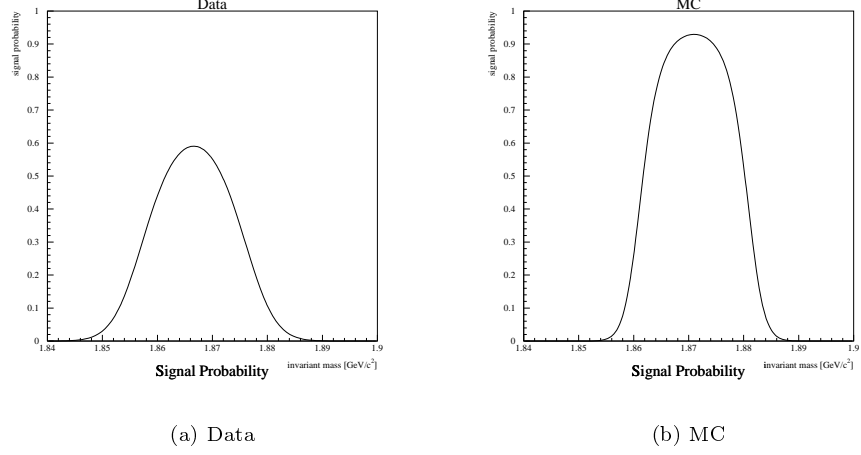(a) Data   (b) MC

Figure 3.7: The signal probability distributions of D^+ candidates for the data and MC samples.

In general the resolution term can be represented by a Gaussian function;

$$G\left(t|\sigma\right) \equiv \frac{1}{\sqrt{2\pi}\sigma} \exp\left(-\frac{t^2}{2\sigma^2}\right) . \qquad (3.12)$$

I calculate the error of the proper time $\sigma_{t,i}$ due to the detector resolution event by event. Since proper time t is the function of $\vec{\eta} = (\vec{r}_{\mathrm{dec}}, \vec{r}_{\mathrm{IP}}, \vec{p})$, the error of the proper time σ_t is given in equation (3.13).

$$\sigma_t = \left(\frac{\partial t}{\partial \vec{\eta}}\right)^T E_\eta \left(\frac{\partial t}{\partial \vec{\eta}}\right) \qquad (3.13)$$

$$E_\eta = \begin{pmatrix} E_{\mathrm{dec}} & 0 & 0 \\ 0 & E_{\mathrm{IP}} & 0 \\ 0 & 0 & E_p \end{pmatrix} \qquad (3.14)$$

E_{dec}, E_{IP}, E_p are the error matrices of the D^+ decay vertex, the production point and the D^+ momentum, respectively. The off-diagonal submatrices which correspond to the correlation between $\vec{r}_{\mathrm{dec}}$, $\vec{r}_{\mathrm{IP}}$, and $\vec{p}$ are neglected since σ_t is dominated by E_{dec}. The error of the proper time σ_t is

$$\sigma_t = \frac{m}{c|p_y|} \sqrt{E_{\mathrm{dec}\,yy} + E_{\mathrm{IP}\,yy} + \left(\frac{r_{\mathrm{dec}\,y} - r_{\mathrm{IP}\,y}}{p_y}\right)^2 E_{p\,yy}} . \qquad (3.15)$$

Figure 3.8 shows the σ_t distributions for the D^+ candidates within ± 3 standard deviations around the D^+ mass peak in the data and Monte Carlo samples.

27

(a) Data   (b) MC
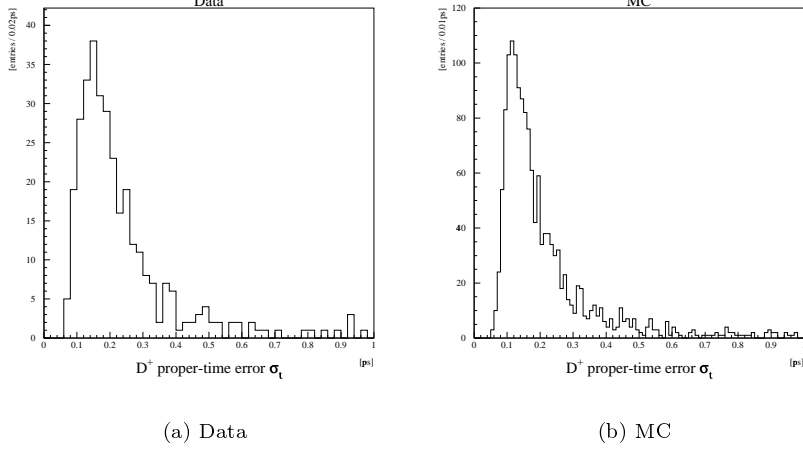
Figure 3.8: The distribution of the error of the proper time σ_t.

Since the error estimation using the method described above is not necessarily perfect I introduce a scaling factor S to take into account systematic under- or over-estimation of the σ_t. This assumption is checked in the section 4.1.

For a small fraction of D^+ candidates f_{mis}, I introduce another Gaussian resolution function with σ_{mis}. This function takes into account the effects such as the hard multiple-Coulomb scattering, pattern recognition errors in the CDC, or wrong SVD-hit association. The calculated and scaled error of the proper time $S\sigma_{t,i}$ underestimates these effects. I assume that the proper-time error for the mis-measured events is distributed symmetrically around the real value and that it is independent of $\sigma_{t,i}$. Combining both Gaussian functions the resolution term is given as;

$$R(t_i - t') = (1 - f_{mis})G(t_i - t'|S\sigma_{t,i}) + f_{mis}G(t_i - t'|\sigma_{mis}). \qquad (3.16)$$

The probability density function becomes

$$\rho(t_i) = \int_0^{\infty} \underbrace{[p_{sig,i}E(t'|\tau_{sig}) + (1 - p_{sig,i})\{f_{\tau_{BG}}E(t'|\tau_{BG}) + (1 - f_{\tau_{BG}})\delta(t')\}]}_{\text{lifetime term}}$$

$$\times \underbrace{[(1 - f_{mis})G(t_i - t'|S\sigma_{t,i}) + f_{mis}G(t_i - t'|\sigma_{mis})]}_{\text{resolution term}} dt'. \qquad (3.17)$$

3.2.3   Fit Results

The proper-time distribution of the D^+ candidates within ± 6 standard deviations around the D^+ mass peak is fitted with unbinned maximum likeli-

28

hood fit using the probability density function described above. Candidates whose proper-time error σ_t is greater than 2 ps or proper time t is not between -4 ps and 6 ps are not used in the fit. The fit results for the data and Monte Carlo samples are summarized in Table 3.6. Figures 3.9 and 3.10 show the D^+

Table 3.6: Result of the fit to the D^+ proper-time distribution.

Parameter	Data	MC
τ_{sig}	0.82±0.13 ps	1.026±0.046 ps
S	1.4±0.2	1.37±0.09
σ_{mis}	2.1±0.4 ps	1.2±0.4 ps
f_{mis}	0.13±0.05	0.04±0.02
τ_{BG}	0.9±0.4 ps	0.95±0.15 ps
$f_{\tau_{BG}}$	0.4±0.1	0.56±0.08

proper-time distributions for the signal dominated region (within ±3 standard deviations around the D^+ mass peak) and the background dominated region ($3\sigma < |m_{K^-\pi^+\pi^+} - m_{D^+}| < 6\sigma$). The fit results are also displayed as solid lines. The data points are well described by the fits for both signal and background dominated regions.

Fit results for τ_{BG} and $f_{\tau_{BG}}$ are quite similar between the data and MC samples. It indicates that background shape in the Monte Carlo sample is similar to that in the data.

The D^+ lifetime obtained in the Monte Carlo sample is 1.026 ± 0.046 ps which is in good agreement with the input value of 1.057 ps. The D^+ lifetime is measured to be $\tau_{D^+} = 0.82 \pm 0.13$ ps. It is consistent with the world average value of $\tau_{D^+} = 1.057 \pm 0.015$ ps within 2 standard deviations.
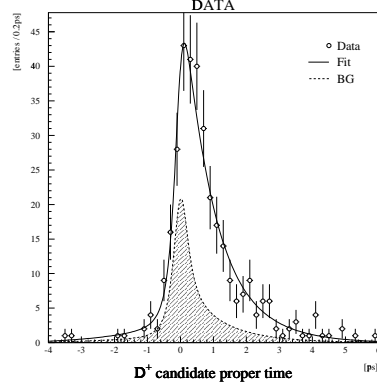
(a) Data (Linear Scale)
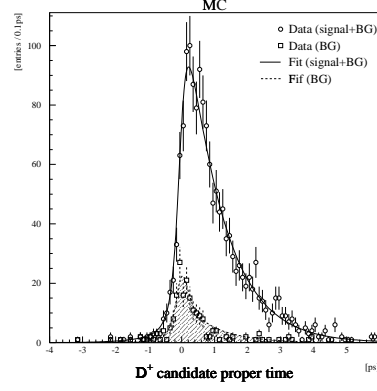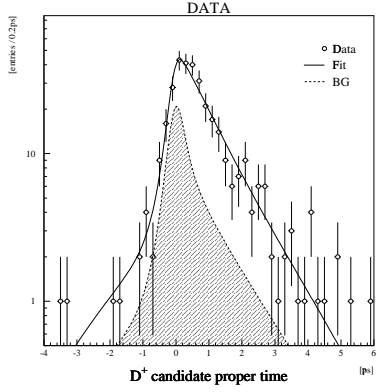
(b) MC (Linear Scale)
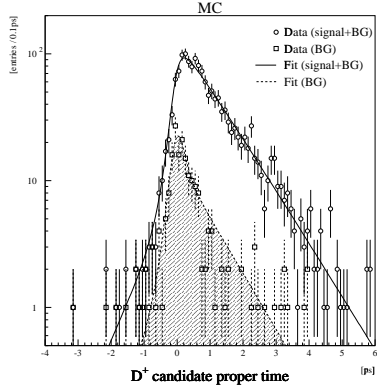
(c) Data (Log Scale)

(d) MC (Log Scale)

Figure 3.9: The proper-time distributions of the D^+ candidates of the data and MC with a mass within $\pm 3\sigma$ around D^+ mass peak plotted on a linear scale and on a logarithmic scale. Points with error bar represents data. A solid line represents the fit result. A dashed line represents the background function.
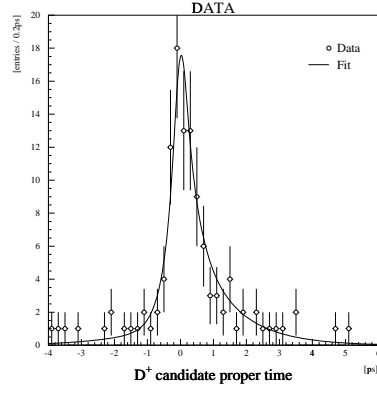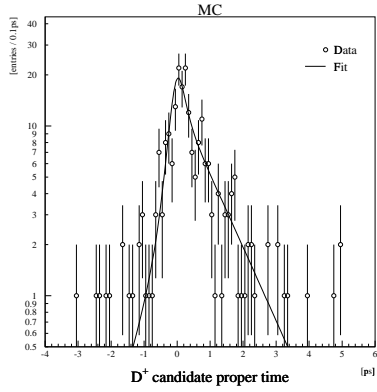
(a) Data (Linear Scale)
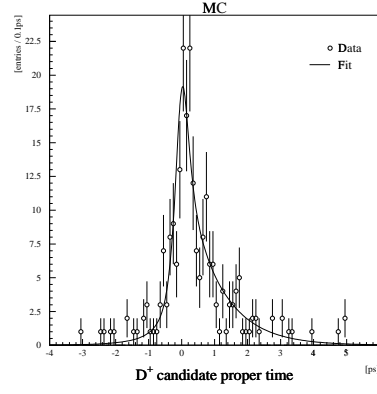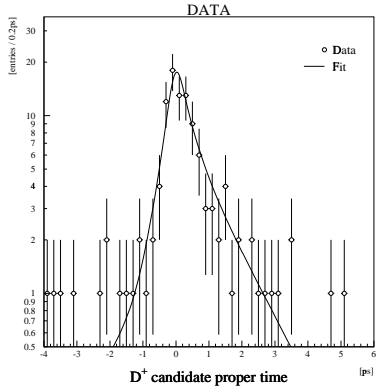
(b) MC (Linear Scale)

(c) Data (Log Scale)

(d) MC (Log Scale)

Figure 3.10: The proper-time distributions of the D^+ candidates of the data and MC in the sideband region ($3\sigma < |m_{K^-\pi^+\pi^+} - m_{D^+}| < 6\sigma$) on a linear scale and on a log scale. Points with error bar represents data. A solid line represents the fit result.

Chapter 4

Systematics Study

In this chapter, systematic bias of the analysis is evaluated using Monte Carlo sample.

I compare the measured values with the values generated in the MC for the D^+ decay vertex point, production point and proper time. Systematic bias in the D^+ proper time calculation is evaluated in this study. The proper-time dependence of the D^+ reconstruction efficiency is also studied.

The lifetime fit procedure is also examined. MC samples with different D^+ lifetimes are generated and the results of the lifetime fits are compared with the input values. The effect of the wrong estimation of the IP size on the lifetime fit is also studied.

4.1   Reconstruction

The D^+ decay vertex is reconstructed from $K^- \pi^+ \pi^+$ tracks using kinematic vertex constraint fit. The difference between the reconstructed vertex position ($\vec{r}_{\mathrm{rec}}$) and the generated vertex position ($\vec{r}_{\mathrm{gen}}$) (the residual of the vertex) in y coordinate is plotted in Figure 4.1(a). The residual distribution is fitted with a sum of two Gaussians with a same mean value;

$$\rho(x) = A \left[\frac{f}{\sqrt{2\pi}\sigma_1} \exp\left\{ -\frac{(x-\mu)^2}{2\sigma_1^2} \right\} + \frac{1-f}{\sqrt{2\pi}\sigma_2} \exp\left\{ -\frac{(x-\mu)^2}{2\sigma_2^2} \right\} \right]. \quad (4.1)$$

Fit results are listed in Table 4.1. The fit yields $\sigma_1 \sim 38\,\mu\mathrm{m}$ for the core Gaussian. The core Gaussian contains $\sim 67\,\%$ of the D^+ candidates. The resolution of the D^+ decay vertex is about $60\,\mu\mathrm{m}$. (This is the weighted average of the σ of the core and wide Gaussians.) Figure 4.1(b) shows the distribution of the difference between the reconstructed and generated vertex positions divided by the calculated error for each vertex, i.e. the pull of the vertex, in y coordinate. If the calculated error for each vertex is correct the pull distribution should be a Gaussian with $\sigma = 1$. It seems valid to introduce of the scaling factor for the
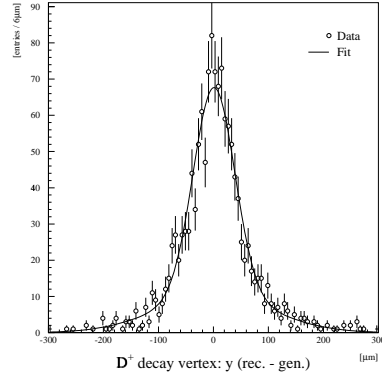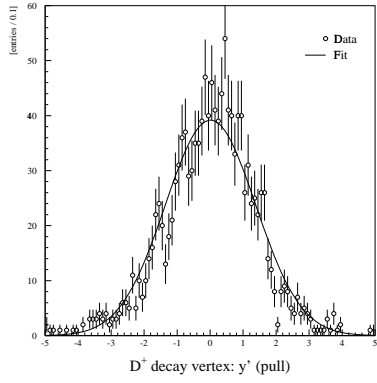
(a) Residual y (b) Pull y
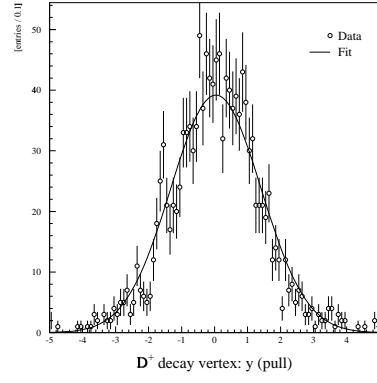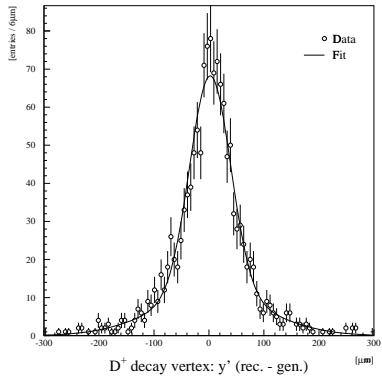
(c) Residual y' (d) Pull y'

Figure 4.1: The residual and pull distributions for the $D^+ \rightarrow K^- \pi^+ \pi^+$ vertex reconstruction in y and y' coordinates.

Table 4.1: The fit results for the residual and pull distributions of the D^+ decay vertex.

Parameter	Residual y	Pull y	Residual y'	Pull y'
μ	$1.0\pm1.4\,\mu$m	0.04 ± 0.04	$2.3\pm1.4\,\mu$m	0.01 ± 0.04
σ_1	$38\pm3\,\mu$m	1.37 ± 0.03	$37\pm3\,\mu$m	1.37 ± 0.03
A	1344 ± 37	1345 ± 37	1344 ± 37	1345 ± 37
σ_2	$104\pm8\,\mu$m	—	$103\pm7\,\mu$m	—
f	0.67 ± 0.06	—	0.67 ± 0.05	—
χ^2/DOF	$86/74$	$117/83$	$61/75$	$149/84$

resolution term in the lifetime fit since the pull distribution does not show a large non-Gaussian tail. The pull distribution is fitted with a Gaussian;

$$f(x) = \frac{A}{\sqrt{2\pi}\sigma_1} \exp\left\{ -\frac{(x-\mu)^2}{2\sigma_1^2} \right\}. \tag{4.2}$$

The fit results are also listed in Table 4.1. The distribution is centered around zero but have $\sigma \sim 1.4$ instead of 1.0. This is consistent with the scaling factor of 1.4 obtained from the lifetime fit for the MC sample.

To study the reconstruction bias along the D^+ flight direction, I introduce a new coordinate y' which is defined for each candidate as

$$y' \equiv \frac{p_y}{|p_y|}y. \tag{4.3}$$

In the new coordinate the proper time in equation (3.7) is expressed as

$$t = \frac{m}{c} \frac{(r_{\text{dec}\,y'} - r_{\text{IP}\,y'})}{|p_{y'}|} \tag{4.4}$$

where $(r_{\text{dec}\,y'} - r_{\text{IP}\,y'})$ in the numerator equals to the D^+ flight length along y axis. The residual and pull distributions in y' coordinate are plotted in Figure 4.1(c) and 4.1(d), respectively. The residual distribution is fitted with a sum of two Gaussians with a same mean value (equation (4.1)). The pull distribution is fitted with a Gaussian (equation (4.2)). The fit results are listed in Table 4.1. No bias is observed in those distributions.

The bias in the D^+ production point is also studied in a similar manner as above. Figure 4.2 shows the residual and the pull distributions of the D^+ production point in y and y' coordinates. Both distributions are fitted with a Gaussian since they do not show non-Gaussian tail. The fit results are listed in Table 4.2. Both residual and pull distributions in y and y' coordinates are centered around zero. The resolution of the production point is about $15\,\mu$m. This is consistent with the fact that this MC sample is generated with the IP size in y coordinate $\sigma_y = 15\,\mu$m and that the correct IP size is put into the reconstruction program. The σ of the pull distribution is consistent with 1.0. It
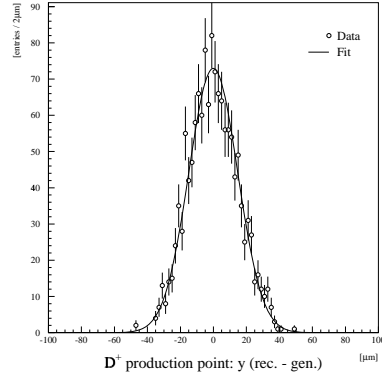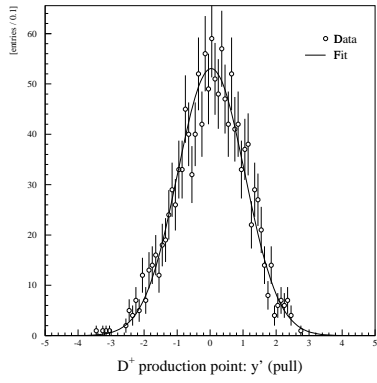
(a) Residual y (b) Pull y
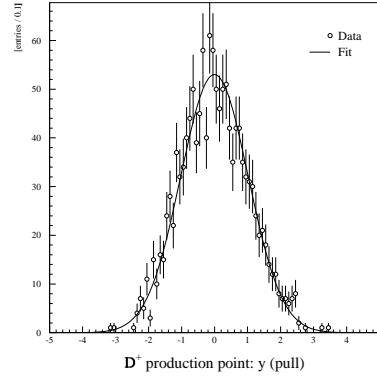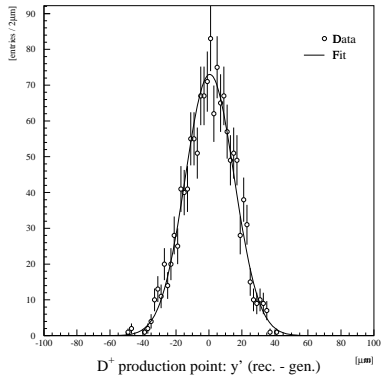
(c) Residual y' (d) Pull y'

Figure 4.2: The residual and pull distributions for the D^+ production point reconstruction in y and y' coordinates.

Table 4.2: The fit results for the residual and pull distributions of the D^+ production point.

Parameter	Residual y	Pull y	Residual y'	Pull y'
μ	$-0.09\pm0.40\,\mu$m	-0.004 ± 0.028	$0.5\pm0.4\,\mu$m	0.03 ± 0.03
σ_1	$14.8\pm0.3\,\mu$m	1.02 ± 0.02	$14.8\pm0.3\,\mu$m	1.02 ± 0.02
A	1356 ± 37	1356 ± 37	1356 ± 37	1356 ± 37
$\chi^2/$DOF	$33/38$	$46/53$	$42/39$	$44/53$

indicates that the production point reconstruction method gives the correct error when the IP profile is known properly. Since the resolution of the production point ($\sim 15\,\mu$m) is very small compared with the resolution of the decay vertex ($\sim 60\,\mu$m), the proper-time error is dominated by the decay-vertex error.

The residual and pull distributions of the D^+ proper time are shown in Figure 4.3. The residual distribution is fitted with a sum of two Gaussians with
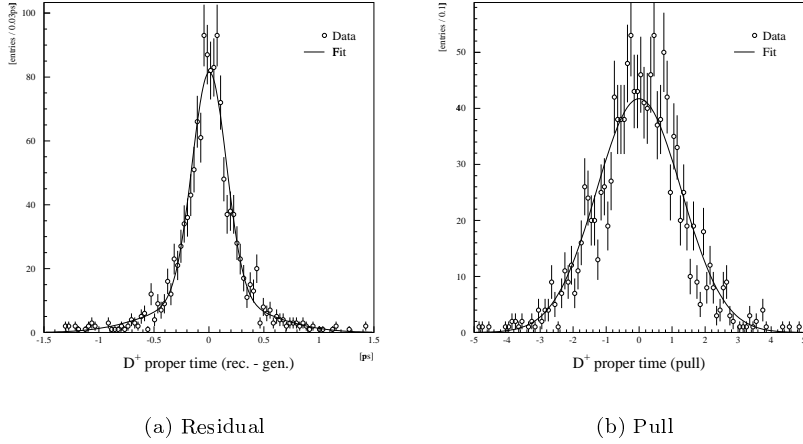
(a) Residual (b) Pull

Figure 4.3: The residual and pull distributions for the D^+ proper-time calculation.

a same mean value and the pull distribution is fitted with a Gaussian. The fit results are summarized in Table 4.3. The residual and pull distributions are centered around zero and no bias is seen in the proper-time calculation. The proper-time resolution for the core Gaussian is ~ 0.16 ps. The core Gaussian contains 69 % of the D^+ candidates. The pull distribution has $\sigma \sim 1.3$ instead of 1.0.

The proper-time dependence of the D^+ reconstruction efficiency is also stud-

Table 4.3: The fit results for the residual and pull distributions of the D^+ proper time.

Parameter	Residual t	Pull t
μ	0.004±0.006 ps	−0.003±0.035
σ_1	0.155±0.009 ps	1.29±0.02
A	1345±37	1346±37
σ_2	0.49±0.03	—
f	0.69±0.04	—
χ^2/DOF	93/72	167/80

ied. Figure 4.4 shows the D^+ reconstruction efficiency as a function of the D^+ proper time. No systematic dependence is observed.
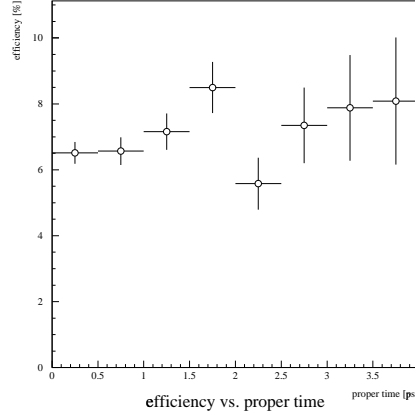
Figure 4.4: The efficiency of the D^+ reconstruction versus the D^+ proper time.

4.2 Lifetime Fit

Systematic effects associated with lifetime fit are studied in this section.

I generate three signal Monte Carlo samples with different D^+ lifetimes (τ_{D^+} = 0.5287 ps, 1.057 ps, and 1.586 ps). Only signal part of the probability density function in equation (3.17) is used for the lifetime fit. Results of the lifetime fits for the three samples are summarized in Figure 4.5. The lifetime fit yields consistent results with the input values. It indicates the lifetime fit procedure and the probability density function in the fit contain no significant problem.
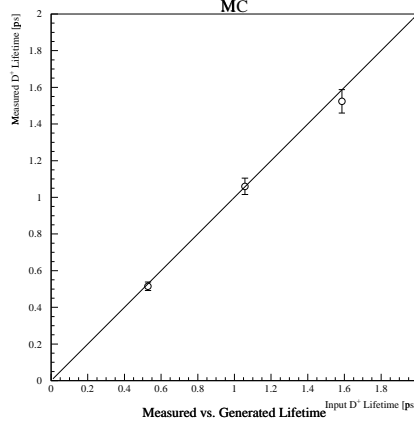
Figure 4.5: The fitted D^+ lifetimes in the signal Monte Carlo samples compared with the input value.

I also study the dependence of lifetime fit on the wrong estimation of the IP size. The MC sample is generated with $\tau_{D^+} = 1.057$ ps, the IP size of $\sigma_x = 110\,\mu$m and $\sigma_y = 5\,\mu$m. Different IP sizes are assumed in the analysis and the results are compared. Results with different σ_x values are summarized in Table 4.4. Results with different σ_y values are summarized in Table 4.5. The results

Table 4.4: Fit results with different σ_x assumptions for the D^+ production point reconstruction.

| input σ_x	$70\,\mu$m	$110\,\mu$m	$150\,\mu$m
τ_{sig}	1.063±0.046 ps	1.060±0.045 ps	1.063±0.048 ps
S	1.2±0.1	1.2±0.1	1.2±0.1
σ_{mis}	0.37±0.19 ps	0.37±0.18 ps	0.38±0.17 ps
f_{mis}	0.10±0.11	0.10±0.11	0.09±0.10

indicate that wrong estimation of the IP size does not cause mismeasurement of the D^+ lifetime.

Figure 4.6 and 4.7 shows correlations of the τ_{sig} with S, σ_{mis}, f_{mis}, τ_{BG} and $f_{\tau_{BG}}$ for the data and MC samples. All background related parameters for the data show significant correlations while those for the MC show little correlations. Background rejection should be improved to reduce the correlation.
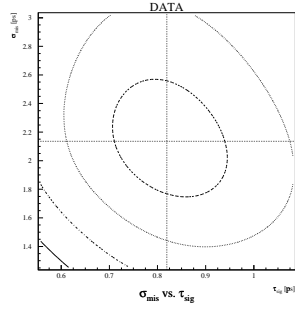
In conclusion no significant systematic bias exist in the analysis of D^+ lifetime.
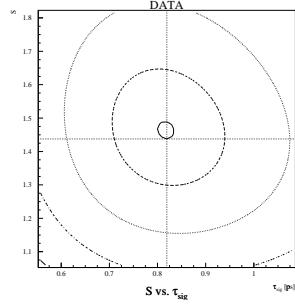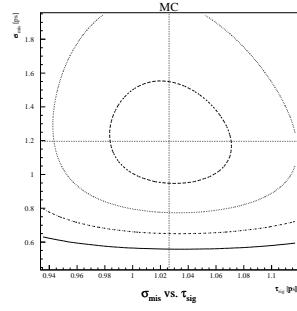
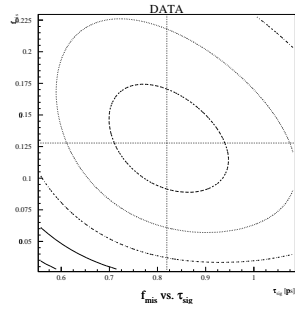(a) S vs. τ_{sig} (Data)　　　　(b) S vs. τ_{sig} (MC)
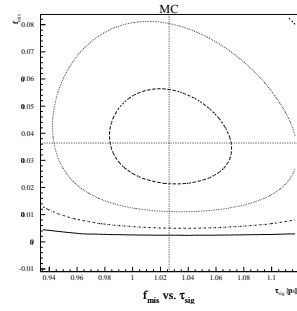
(c) σ_{mis} vs. τ_{sig} (Data)　　　　(d) σ_{mis} vs. τ_{sig} (MC)
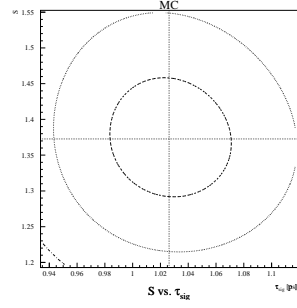
(e) f_{mis} vs. τ_{sig} (Data)　　　　(f) f_{mis} vs. τ_{sig} (MC)

Figure 4.6: Correlation of τ_{sig} with each fit paramater (S, σ_{mis} and f_{mis}).

Table 4.5: Fit results with different σ_y assumptions for the D^+ production point reconstruction.

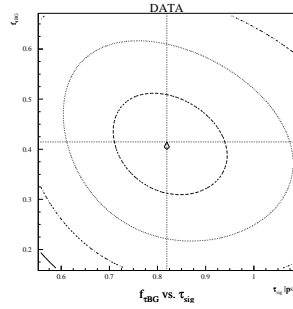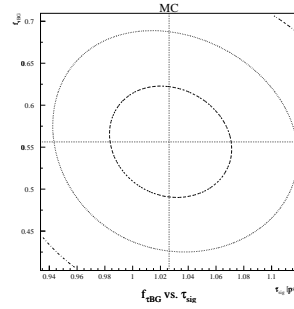| input σ_y	$2\,\mu$m	$5\,\mu$m	$10\,\mu$m
τ_{sig}	1.063±0.045 ps	1.060±0.045 ps	1.066±0.045 ps
S	1.2±0.1	1.2±0.1	1.2±0.1
σ_{mis}	0.39±0.17 ps	0.37±0.18 ps	0.32±0.15 ps
f_{mis}	0.08±0.10	0.10±0.11	0.15±0.17

(a) τ_{BG} vs. τ_{sig} (Data)

(b) τ_{BG} vs. τ_{sig} (MC)
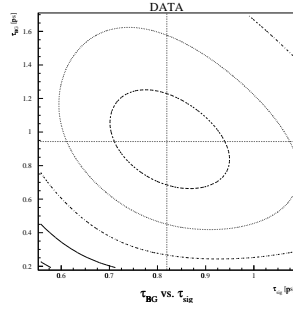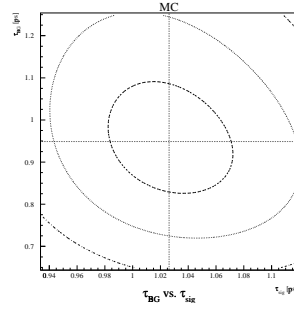
(c) $f_{\tau_{BG}}$ vs. τ_{sig} (Data)

(d) $f_{\tau_{BG}}$ vs. τ_{sig} (MC)

Figure 4.7: Correlation of τ_{sig} with each fit parameter (τ_{BG} and $f_{\tau_{BG}}$).

Chapter 5

Conclusion

I measure the D^+ lifetime based on the data taken with the BELLE detector. It is measured to be

$$\tau_{D^+} = 0.82 \pm 0.13 (\text{stat}) \, \text{ps}.$$

According to the Particle Data Group[1] the world average of the D^+ lifetime is

$$\tau_{D^+}(\text{world average}) = 1.057 \pm 0.015 \, \text{ps}.$$

My measurement is smaller than the world average but within 2 standard deviations. Systematic biases are studied for the proper-time calculation and the lifetime fit. No bias or problem is found.

D^+ candidate selection should be optimized to improve signal-to-background ratio. Much more data is also required to improve statistical error of the lifetime measurement.

I plan to measure the lifetimes of other charmed mesons (D^0 and D_s^+). I also plan to estimate the systematic error for the lifetime measurement. Finally the lifetime measurement should be performed in z direction to evaluate the vertexing performance in z direction.

Acknowledgement

Appendix A

Analysis Tools

A.1 Kinematic Fit

Kinematic fit[5] is based on the least square method of χ^2 using the Lagrange multiplier method.

In a vertex constraint fit the constraint equations are obtained from the equations of motion of each track assuming that all the tracks come from a common vertex $\vec{v}$. These constraints are incorporated using the method of Lagrange multipliers. The large errors (covariant matrix L) are assigned to initial values of the parameters $\vec{v}$ and the limit $L \rightarrow \infty$ is taken for the calculation.

In a mass constraint vertex fit another constraint equation

$$\left(\sum_i E_i \right)^2 - \left(\sum_i \vec{p}_i \right)^2 - m^2 = 0$$

is used in addition to the constraints for the vertex fit. E_i and $\vec{p}_i$ are the energy and momentum of the ith track, respectively. m is the invariant mass.

In a vertex constraint fit with IP constraint the mean position and size of the interaction point are assigned as the initial value of the common vertex $\vec{v}$ and the error of the parameter $\vec{v}$ in the form of the covariant matrix L, respectively.

A.2 Particle ID

The particle identification (PID) for the BELLE is based on the three detector informations :

- dE/dx information from the CDC

- TOF information

- ACC information

The detail of each detector is described in section 2.2.

The PID probability is calculated as follows. First, each device provides the probability for the electron e, the muon μ, the pion π, the kaon K, and the proton p for each track. The CDC measures dE/dx and the probability of a track being a particular particle type i ($=e$, μ, π, K, p) is calculated as

$$\mathrm{P}_i(\mathrm{CDC}) = \frac{1}{\sqrt{2\pi}\sigma_{dE/dx}^i} \exp\left\{ -\frac{1}{2}\left(\frac{dE/dx_{mea} - dE/dx_{exp}^i}{\sigma_{dE/dx}^i}\right)^2\right\}$$

where dE/dx_{mea} is measured dE/dx, dE/dx_{exp}^i is the expected one for the particle type i, and $\sigma_{dE/dx}^i$ is the resolution of measured dE/dx. The TOF measures the time-of-flight and the probability is calculated in a similar manner as CDC with measured and expected time-of-flight. And the ACC detects the Čerenkov light and the probability is calculated as

$$
\begin{aligned}
\mathrm{P}_i(\mathrm{ACC}) &= \epsilon_{exp}^i \ (\text{detected}) \\
\mathrm{P}_i(\mathrm{ACC}) &= (1 - \epsilon_{exp}^i) \ (\text{not detected})
\end{aligned}
$$

where ϵ_{exp}^i is the expected detection efficiency for the particle hypothesis of i. Next, the combined probability P_i is calculated as

$$\mathrm{P}_i = \mathrm{P}_i(\mathrm{ACC}) \times \mathrm{P}_i(\mathrm{TOF}) \times \mathrm{P}_i(dE/dx)$$

Then the relative ratio of P_i is used. For example, the kaon probability against pion $\mathrm{prob}(K)$ is calculated as

$$\mathrm{prob}(K) = \frac{\mathrm{P}_K}{\mathrm{P}_K + \mathrm{P}_\pi}.$$

Bibliography

[1] Particle Data Group, *"Review of Particle Physics"*, Eur. Phys. J. C3, 1(1998)

[2] *"KEKB B-Factory Design Report"*, KEK Report 95-7.

[3] *"A study of CP violation in B meson decays - technical design report -"*, KEK Report 95-1.

[4] M.Yokoyama *et al.*, *"Measurement of radiation effects on VA1 chip"*, BELLE note #196.

[5] J.Tanaka, *"Kinematic Fitting"*, BELLE note #194